Microstructural investigation of IASCC crack tips extracted from thimble tube O-ring specimens

Microstructural investigation of IASCC crack tips extracted from Thimble Tube O-ring specimens

A. G. Penders[a,b,1,*], M. J. Konstantinović[a], T. Yang[b,1,2], R-W. Bosch[a], D. Schryvers[b,1], F. Somville[c]

[a] *Studiecentrum voor Kernenergie - Centre d'Etude l'Energie Nucléaire (SCKCEN), Boeretang 200, B-2400 Mol, Belgium*
[b] *University of Antwerp, Groenenborgerlaan 171, 2020 Antwerp, Belgium*
[c] *ENGIE-Tractebel Engineering, Boulevard Simon Bolivar 34-36, 1000 Brussels, Belgium*

Abstract

The microstructural features of intergranular irradiation-assisted stress corrosion crack tips from a redeemed neutron-irradiated flux thimble tube (60 dpa) have been investigated using focused-ion beam analysis and (scanning) transmission electron microscopy. The current work presents a close examination of the deformation field and oxide assembly associated with intergranular cracking, in addition to the analysis of radiation-induced segregation at leading grain boundaries. Evidence of stress induced martensitic transformation extending from the crack tips is presented. Intergranular crack arrest is demonstrated on the account of the external tensile stress orientation, and as a consequence of MnS inclusion particles segregating close to the fractured grain boundary. Exclusive observations of grain boundary oxidation prior to the cracking are presented, which is in full-agreement with the internal oxidation model.

Keywords: IASCC, 316SS, neutron-irradiation, flux thimble tube, (S)TEM, FIB, internal oxidation,

1. Introduction

Nuclear reactor power plant (NPP) internal components experience material property changes during service operation due to a complex interaction of several material degradation phenomena [1, 2, 3, 4, 5]. This degradation includes changes in the material microstructure and microchemistry under irradiated conditions, which can ultimately lead to intergranular irradiation assisted stress corrosion cracking (IASCC) [6, 7, 8, 9, 10]. The prime example of IASCC is the cracking of baffle to former bolts (BFBs), which has been observed for the first time in 1989 in French NPPs. Since then, similar trends of progressive BFB cracking have been observed in other NPPs, including those in the USA, Japan, and Belgium. The susceptibility to cracking is considered to evolve as a consequence of correlating in-service reactor conditions, and is therefore limiting the integrity of NPP operations after extended periods of operation. The

*This article is the result of a research project funded by ENGIE Electrabel.
*Corresponding author
Email addresses: apenders@sckcen.be (A. G. Penders), mkonstantinovic@sckcen.be (M. J. Konstantinović), tong.yang@uantwerpen.be (T. Yang), rik-wouter.bosch@sckcen.be (R-W. Bosch), nick.schryvers@uantwerpen.be (D. Schryvers), frederic.somville@tractebel.engie.com (F. Somville)
URL: https://www.sckcen.be/ (A. G. Penders), https://www.uantwerpen.be/en/research-groups/emat/ (A. G. Penders)
[1] Electron Microscopy for Materials Science - EMAT
[2] On leave from State Key Laboratory of Powder Metallurgy, Central South University, Changsha 410083, China

factors that ultimately lead to intergranular failure primarily include the aspect of external stresses on susceptible materials subjected to a corrosive environment while under the influence of intense neutron-irradiation. IASCC envelops a complex interplay between common elements such as stress, material composition, temperature, and water chemistry. Contemporary investigations have led to a more in-depth focus on the interdependencies between underlying correlating mechanisms related to IASCC, rather than indicating a single responsible failure mechanism for the observed failures.

To investigate the phenomenon of intergranular SCC (IGSCC), a substantial amount of research has been devoted to the microstructural and microchemical evolution of structural component materials subjected to neutron-irradiation. Irradiated stainless steels primarily experience radiation damage as consequence of atomic displacement, which may lead to radiation-induced changes in the microstructure. Typical nucleation of defect clusters entail the formation of dislocation and Frank loops, black spots, precipitates, and voids [11]. In substantial concentrations, these defects cause a significant change in the material's mechanical and fracture properties, which can be ultimately associated with a strong increase in IASCC susceptibility. Concurrent with radiation-induced hardening and embrittlement, key potential contributors to intergranular failure entail radiation-induced segregation (RIS) [12, 4, 13, 14] at leading grain boundaries and plastic strain-localization [15, 16] in correspondence to the cracking mechanism. The former implicates the preferential segregation or depletion of structural and solute elements at grain boundaries and other microstructural sinks. Bruemmer et al. [12, 4] illustrated a strong correlation between a low grain boundary Cr-content and increased IGSCC susceptibility, while the influence of minor elements may additionally increase the crack growth rates [14]. However, Busby et al. [13] has called into question the role of RIS by comparing proton-irradiated and post-irradiation specimens, illustrating that RIS of any one element cannot be solely responsible for intergranular failure. On the other hand, strain localization describes how plastic strain is restricted into narrow discontinuous clear channels, often terminating at the grain boundary. Such clear channels arise from the annihilation of the aforementioned defect clusters and provide a preferential path for subsequent dislocation motion to occur. Interaction of these dislocations may exert a localized increase in stress at the grain boundary. This can be linked to both grain boundary separation [15] and sliding [16] when caused by dislocation channels and common dislocation slip, respectively. However, clear channels are not commonly observed in high dpa stainless steels, which casts some doubt upon their relevance for IASCC cracking in heavily irradiated materials.

Clearly, despite a lot of effort, no consensual interpretation for IASCC failure has yet been agreed upon. To that end, it is imperative to inquire more about the physical and chemical characteristics of crack initiation in susceptible materials. Though, as operating with irradiated materials is both difficult and expensive, little microscopical studies on neutron-irradiated cracks have been

presented so far [17, 18, 19, 20, 21]. The emerging picture from available observations does suggest that intergranular oxide penetration enhances the cracking susceptibility under tensile stress [10], a factor which is strongly tied to the localized deformation close to the crack tip [22, 23]. Lozano-Perez et al. [24] showed that fast-diffusion paths, for instance along microstructural defects such as deformation bands and heavily dislocated structures, accelerate the oxidation process that may embrittle the boundary setting up to the requirements for cracking. Typically, the penetrating oxide is comprised of both a chromite spinel with secondary magnetite precipitates occurring within the crack openings [25]. Cr-depletion may on the one hand facilitate interstitial oxygen transport along the grain boundary to set the stage for embrittlement [26], while on the other hand produce a chromium-depleted spinel oxide which may be prone to cracking due to its low chromium content [10]. Metallic Ni-enrichment ahead of oxidized crack tips has been attributed to either de-alloying [27], or to the higher diffusivity of other structural elements in the corrosion processes [28, 29]. Martensitic transformations have been observed in finite-volumes adjacent to the crack and fracture surfaces which were likely produced during crack propagation and not due to prior cold-work [17, 30, 31, 32]. Amongst the possible orientation relationships between face-centered cubic (fcc) γ-austenite and body-centered cubic (bcc) α'-martensite [33], typically the Kurdjumov-Sachs (K-S) [34] and Nishiyama-Wasserman (N-W) [35] relationships are widely reported. Microstructural observations typically report the nucleation of intermediate hexagonal-close packed (hcp) ϵ-martensite in ways of indirect transformation to bcc martensite laths [36, 31], although direct transformation from the parent austenite phase has been observed on similar accounts [32]. After nucleation, transformed martensite laths may severely contribute to local hardening and strain-localization by impeding on the dislocation glide in the retained austenite phase [36, 37]. On that account, it should be considered that deformation-induced phase transformations close to the crack tip may act as key contributors to intergranular crack propagation.

This work lies in the continuation of the framework set out by Bosch et al. [38], wherein over 80 O-ring specimens were readily cut from a neutron-irradiated 316 stainless steel (SS316) flux thimble tube retrieved from the commercial Tihange PWR NPP reactor in Belgium. Subsequent O-ring compression tests led to an increased understanding of the mechanisms related to IASCC [38, 39]. Additional microscopical analysis of radiation-induced defect structures was performed in relation to post-irradiation annealing experiments on similar type of O-rings [40]. In continuation of this framework, a methodology was developed for the extraction and microstructural analysis of IASCC crack tips using focused ion beam (FIB) analysis and transmission electron microscopy (TEM). Such investigations are considered to be very challenging due to the large intergranular branching nature observed at highly irradiated materials. Still, the current study presents the analysis of one particular 60 dpa neutron-irradiated O-ring that illustrated clear intergranular failure characteristics. The aim of this work is three-fold: (i) to illustrate a working FIB methodology

for crack tip extraction, (ii) to identify microstructural features that can be related to crack initiation and propagation by performing a detailed study of the crack and crack tip morphology, and (iii) to provide additional data to help elucidate on existing cracking mechanisms. This work additionally supports the development of a predictive methodology of IASCC cracking, and for baffle bolt cracking in particular.

2. Materials and methods

2.1. Sample preparation

In recent times, a 316L cold-worked stainless steel flux thimble tube was decommissioned from the Belgian PWR NPP Tihange 2, which remained operational for about 25 years. Tab. 1 illustrates the 316L material composition, which is comparable to the ASTM specification standards and to other flux thimble tube materials reported within the framework of the international IASCC committee program [41]. The tube was cut along its length to create many O-ring specimens of various dosage profiles dependent on where they were extracted from the tube. These O-rings were machined so that any additional crack initiation sites were removed, while still preserving the original in-service reactor oxide layer. Thereafter, constant load SCC tests were performed in a hot cell autoclave, equipped with a tensile loading unit, capable of simulating a PWR environment at 320 °C. The testing procedure and experimental results have been outlined in detail by Bosch et al. [38].

For the purpose of this study, a 60 dpa irradiated O-ring that failed into five majorly connected pieces post constant load testing was selected for microscopical analysis, see Fig. 1. The O-ring received the generic name TTO-1-053 and its testing parameters are presented in Tab. 2 and reference [38]. The specimen was chosen in view of the fact that both primary fracture surfaces post testing exhibited a full intergranular fracturing mode under scanning electron

Table 1: Chemical composition of Tihange thimble tube O-ring specimens made from 316L cold-worked (20% CW level) stainless steel.

	Fe	**Ni**	**Cr**	**Mo**	**S**	**P**	**Si**	**Mn**	**Co**	**C**
Comp (wt. %)	Bal.	12.8	17.0	2.68	0.009	0.022	0.53	1.79	0.07	0.044

Table 2: TTO-1-053 SCC test matrix of autoclave test conditions simulating PWR atmosphere at 320 °C.

Specimen	**Length (mm)**	**Water chemistry**	**Dose (dpa)**	σ_y **(MPa)**	**Stress (MPa)**	**Time-to-failure (h)**
TTO-1-053	10.425	2 ppm Li 1000 ppm B 30 cm^3/kg H_2	60	1000	392	1910

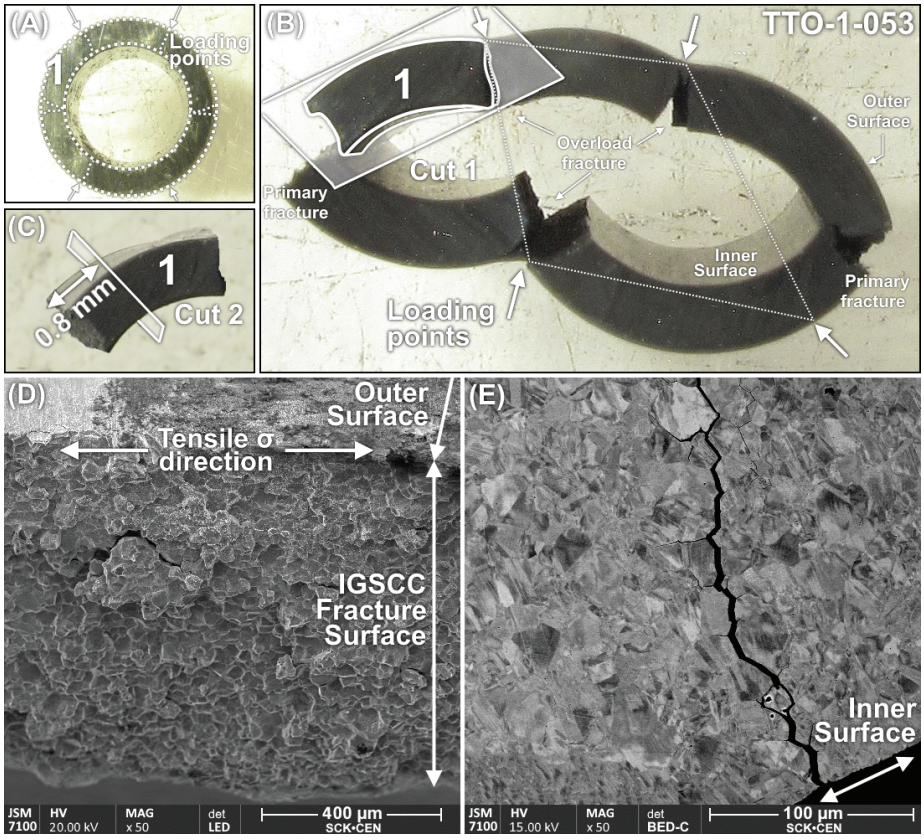

Figure 1: TTO-1-053 sample preparation. (A) Intact O-ring specimen prior to constant load testing. (B) O-ring post constant load compression testing. Indications of the loading points and traversal cut along the middle of the specimen are depicted. (C) Second cut of the remaining piece, close to the primary fracture surface. (D) Secondary electron SEM view of the fracture surface illustrating the full intergranular mode. (E) Backscattered electron SEM view in edge-on orientation illustrating the extent of branched cracking from the inner surface.

microscopy (SEM) investigation. Additionally, a substantially branched cracking appearance on the O-ring's outer surface was observed. The intergranular cracking nature is demonstrated in cross-sectional and edge-on orientation for the largest piece, see Figs. 1D-E respectively. Backscattered secondary electron (BSE) imaging provides excellent channeling contrast for the visualization of the individual grains which are of the order of several square micrometers. Interestingly, cracks with lengths well beyond the typical grain size may develop equally on the outer as well as on the inner surface of the bulk material. Crack initiation on the inner surface could not be fully excluded, in particular at the regions where high von Mises stress associated to the applied load are present. The latter remains remarkable due to the fact that the inner surface of the thimble tube has been oxidized considerably less while being in contact

with the outside environment (air; 320 °C) rather than PWR atmosphere for the outer surface.

Ultimately, a single piece with a full intergranular fracture surface was retained for further investigation, considering that its fracture surface closely resembled an IASCC-like fracture appearance which clearly did not correspond to any of the overload fractures near the external loading points. In order to reduce the sample activity to reasonable instrument threshold values, the piece was cut according to the specific cutting scheme presented in Figs. 1B and 1C. The final cut was performed in parallel to the fracture surface at a distance of about 0.8 mm. The remaining piece was slightly polished from both sides while still preserving the branched IASCC cracks on the fracture surface, see Fig. 2A.

2.2. FIB analysis

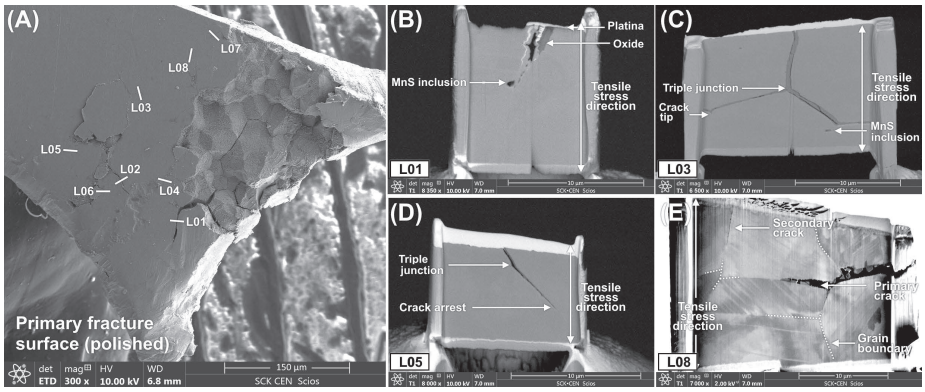

Figure 2: TTO-1-053 FIB specimen preparation from the same primary fracture surface shown in Fig. 1D. (A) Overview of the intergranular fracture surface post cutting operations. (B-E) Backscattered electron (BSE) images of electron-transparent IASCC crack embedded TEM lamellae. (E) FEI's OptiTilt low voltage BSE image demonstrating the leading grain boundary structure. The orientation of compression test autoclave loading unit imposed tensile stress direction is perpendicular towards the lamella surface orientation.

Several IASCC cracks were prepared according to the standard in-situ lift-out technique using the Thermo Scientific Scios DualBeam FIB-SEM. The lift-out procedure for crack extraction was performed in cross-sectional orientation, and has already been demonstrated for the extraction of SCC cracks in duplex materials in one of our previous studies [42]. Lamellae with embedded crack tips were extracted from the bulk specimen and mounted on a copper TEM support grid. Consecutive ion milling steps over a range of various tilt angles, centered around the ion-beam direction on either side of the lamella, ensure a precise and controlled thinning operation in order to create an electron-transparent TEM specimen at the final stages of operation. The ion current is successively reduced after repeated milling iterations between the range of 1 nA down to 0.25

nA. Final low energy cleaning operations at voltages and currents of 5 keV and 0.048 nA, respectively, were applied to remove any Ga^+ ion implantation within the remaining specimen volume.

Tab. 3 presents a total of eight intergranular IASCC cracks readily prepared for microstructural analysis, several of which are depicted in Fig. 2. Interestingly, whereas some cracks may arrest in the bulk or at a later confirmed inclusion particle, other cracks may extend deep down or branch off at a grain boundary triple junction. In relation to the tensile stress direction resulting from the compression testing, it was apparent that all cracks preferably propagated in cleavage mode orientation. Therefore, in the case of tensile stress normal to the cracking plane, the cracks did not come close to full arrest along their oxidized grain boundary. Under these circumstances, cracks extending further than the appropriate TEM lamella size of around 20 μm could not be fully extracted due to geometrical reasons. As such, those fractures were generally not retained for further TEM investigation. In addition, certain lamellae may show signs of extended curtaining [43, 44] due to local aggregated ion milling as a consequence of changes in the material crystal structure, composition, and or irregular topography. Productive steps to minimize the curtaining effect may include FIB-assisted deposition to level the milling surface before the thinning operation starts. However, for the purpose of preserving the initial crack mor-

Table 3: s

Index	**Extracted crack tip (Y/N)**	**Macroscopic stress orientation vs. crack tip orientation**	**Remarks**
L01	Y	//	Crack arrested at an intergranular MnS inclusion particle.
L02*	N	$\perp$	Unarrested crack propagating straight along oxidized grain boundary.
L03	Y	//	Oxidized grain boundaries featuring a crack tip extending from one triple junction.
L04*	N	$\perp$	Unarrested crack branching from oxidized triple junction.
L05	Y	//	Arrested crack propagating straight along oxidized grain boundary.
L06	Y	//	Arrested crack tip extending from heavily corroded grain boundary.
L07*	N	$\perp$	Unarrested crack propagating straight along oxidized grain boundary.
L08	Y	// and $\perp$	Two arrested crack tips, one cleavage crack illustrating multiple branch points and another shearing crack arrested at a triple junction.

phology to the fullest extent, specifically the beam conditions and milling rate were controlled in order to mediate the damage at the final stages of thinning. As a result, certain specimens may be left intentionally thicker to preserve the full integrity of the crack, leaving the final (S)TEM sample thickness varying between $150 - 250$ nm.

2.3. (S)TEM analysis

Conventional and analytical TEM characterization of IASCC crack tips was carried out using the 300 kV JEOL 3010 scanning (S)TEM, equipped with a LaB_6 electron gun and an Oxford Instrument EDS link spectrometer with a corresponding Si(Li) detector. Selected area electron diffraction (SAED) bright (BF-) and centralized dark-field (DF-) TEM imaging were performed in order to characterize the crack morphology, surrounding microstructure, and the oxidized grain boundaries in front of the crack tips. In order to characterize the nanograined oxide, a combination of both rotationally averaging and integrating the corresponding diffraction pattern was employed. This method generates a unique signal from which the interplanar d-ratios can be compared to literature values in order to uniquely characterize the structure. Spot-diffraction patterns encountered within this research were confirmed through the simulation software CrystalDiffract®: a powder diffraction program from CrystalMaker Software Ltd, `www.crystalmaker.com`. Additionally, energy dispersive X-ray spectroscopy (EDS) was performed in combination with diffraction pattern analysis to provide a local chemical composition of the phase structures. The EDS spot analyses were carried out using the smallest attainable spot size, which is estimated to be about 25 nm upon sample infringement. Furthermore, Fresnel underfocus contrast imaging was employed to reveal porous structures and salient fracture bands at the crack tip. Localized fast Fourier transformed (FFT) high-resolution TEM (HR-TEM) diffractograms were utilized to provide additional information regarding the crystallographic structure and largest lattice spacings of the oxide structure. Specifically, this approach applies well for the unique determination of the metal-oxide to oxide phase structures at the crack tip, crack flanks and external oxide surface.

Scanning transmission electron microscopy (STEM) high-angle annular dark field (HAADF) Z-contrast imaging delivers image contrast that scales according to thickness and average atomic number ($I \propto Z^2$) of the specimen, thus providing local chemically-sensitive information of the region of interest. To that end, additional STEM-HAADF imaging of crack tips and leading crack tip grain boundaries were acquired using the aberration-corrected X-FEG Thermo Fisher X-Ant-EM STEM instrument. Spectral maps and line scans were acquired to characterize the local segregation and depletion of structural and minor elements in view of RIS and corrosion processes at the crack tip.

3. Results and discussion

All IASCC cracks extracted from the in-service thimble tube O-ring specimen feature a branched crack morphology characterized by a completely converged crack front and a fully oxidized intergranular fracture surface. Most tips show similar characteristics in terms of morphology and surrounding microstructure. Oxide-filled cracks taper down towards the advanced crack tip, accompanied by strong deformation fields on either side of the grain boundary. General distinctive characteristics include the extensive nature of branching of the intergranular crack morphology, a multi-layered internal oxidation film along the crack flanks, and the presence of long-running microstructural deformation bands extending from the crack flanks towards adjacent grain boundaries. Martensitic laths have been observed adjacent to the crack and leading grain boundary. The oxide structure consists of a primary oxide along the external surfaces and within the crack flanks, while a sparsely precipitated large-grained secondary oxide was observed solely in wide open crack regions some distance away from the actual tip. All investigated cracks exhibit grain boundary oxidation prior to the tip, which gives strong arguments in favor of the internal oxidation mechanism [45, 46, 26, 8, 47] relevant for IASCC.

3.1. Intergranular oxidation

3.1.1. Overview of grain boundary cracking

The extent of intergranular oxidation for a typical IASCC crack branch leading up to a grain boundary triple junction is shown in Fig. 3A. The crack path is characterized by an extensive but brittle branching nature and remains fully developed within the intergranular oxide. The crack mainly follows the metal-oxide interface, as demonstrated in Fig. 3B. Presumably, the applied external stress caused the crack to propagate alongside its weakest interface i.e. strained metal-oxygen bonds, which are inherently more chemically active and thus more prone to cracking than non-strained bonds. Additionally, it is important to express the significance of the three-dimensional aspect of the crack morphology. Certain sections of the crack may subside and/or re-emerge within perspective of the lamella. In addition to the straight cracking nature of the interface, which is followed by an often jagged crack path within the intergranular oxide, these signs are interpreted as a form of brittle crack propagation within the intergranular oxide. Fig. 3C emphasizes on the formation of multiple crack initiation sites within the dense oxidized triple junction. Under closer inspection, these initiation sites may nucleate into numerous brittle microcracks which are formed mostly parallel to the main intergranular crack propagation direction. While under the influence of the external load, these microcracks coalesce into the formation of a fully developed crack front. This observation strongly agrees with the global crack morphology of the main branch. It is believed that the formation of microcracks is of importance to the crack initiation process [39].

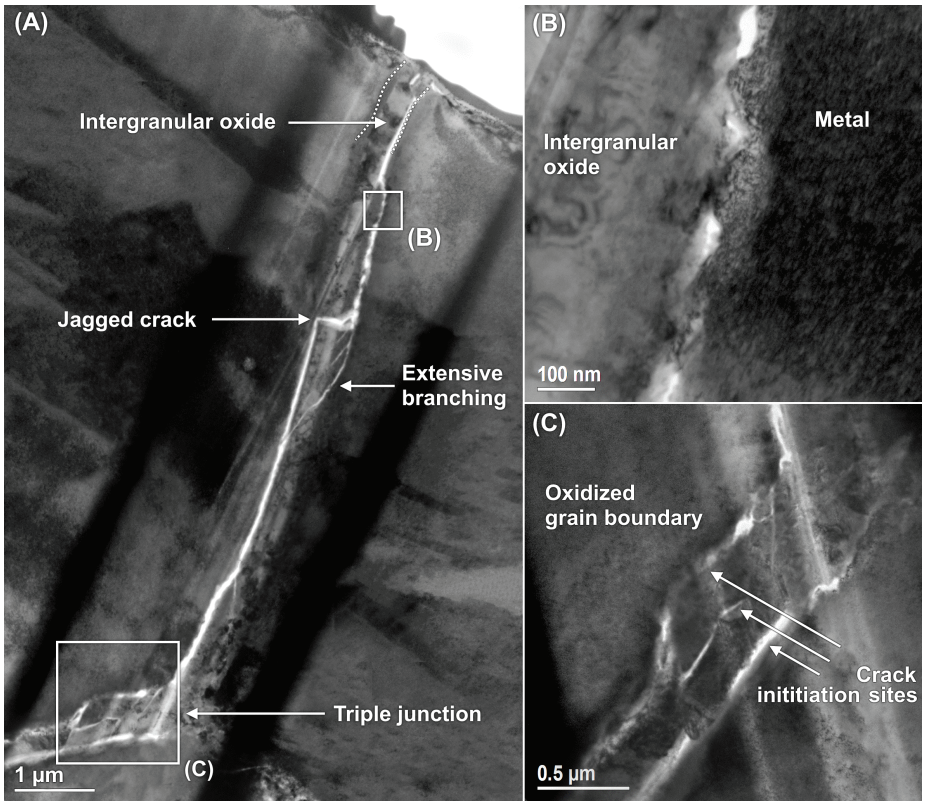

Figure 3: TTO-1-053 L03 (A) BF-TEM overview of a main IASCC branch leading up to a completely oxidized grain boundary triple junction. (B) Magnified view of the metal-oxide interface cracking. (C) Representation of the strong crack branching nature within the intergranular oxide. The darker contrast bands represent intentionally thicker strokes of material that are left behind during the process of FIB-milling in order to mitigate the strong curtaining effect underneath the oxidized triple junction.

3.1.2. Oxide characterization

Additional demonstration of an IASCC crack propagating along the metal-oxide interface is presented in the BF-TEM and DF-TEM overview images presented in Figs. 4A-B. From the DF-TEM view of the intergranular oxide, it is again apparent that the crack favorably propagates alongside the metal-oxide interface, leaving one particular side of the crack flank progressively more oxidized than the other. Its intergranular oxide structure has been examined through diffraction- and EDS-analyzes, see Figs. 4C-E. The attained phase structures are representative for all other intergranular IASCC cracks assessed in this research. From the results, it can be concluded that there is a separation between two different oxides. The entire oxide assembly is constituted of a primary nano-grained crystallite chromium-oxide enriched with a strong iron-rich signal, and a coarse-grained secondary oxide revealing mainly signals of iron and

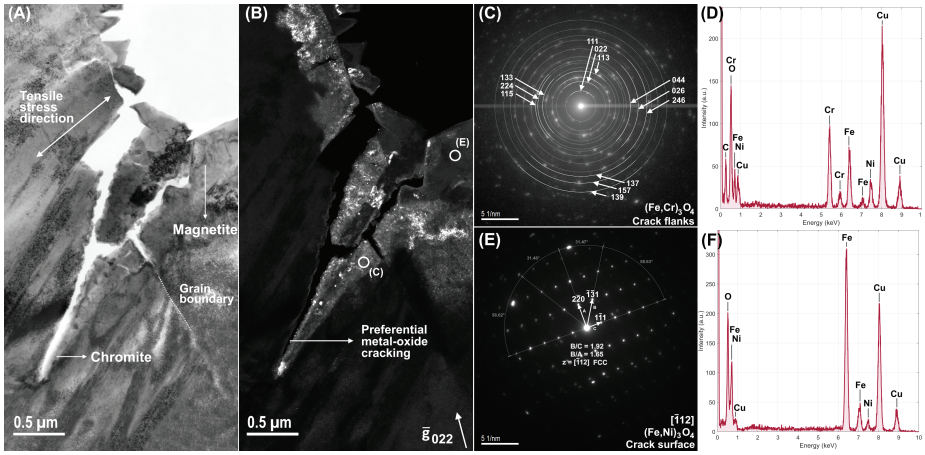

Figure 4: TTO-1-053 L06 (A) BF-TEM and (B) DF-TEM of an IASCC crack imaged from an intergranular oxide reflection. Respectively, the (C,E) diffraction patterns and (D,F) EDS spectra of the corresponding chromite spinel $(Fe,Cr)_3O_4$ and the magnetite deposit $(Fe,Ni)_3O_4$ oxides are depicted. The strong Cu-signal originates from the TEM grid holder.

nickel. Whereas the chromium-rich oxide is homogeneously found around the crack flanks and crack tip, the secondary iron-rich oxide remains sparsely precipitated along the crack flank merely within wide open crack regions. Considering the sole observations of the iron-rich oxide deposits, it is reasoned that this oxide is the resultant of bulk dissolution processes and is consequently precipitated at accessible crack regions exposed to the environment [25].

The most plausible structure corresponding to the main oxide component along the crack flanks is found to be chromite spinel $(Fe,Cr)_3O_4$ with a known lattice parameter of 0.8378 nm [48]. The result is supported by the observed ring-like diffraction pattern originating from the nano-grained structure, featuring a spinel fcc-centering with an experimentally obtained lattice constant of 0.8339 nm, see Fig. 4C. Furthermore, given the strong Cr- and Fe-signals in the corresponding EDS spectrum of Fig. 4D, other candidate oxide structures such as Cr_2O_3 which has been experimentally observed in stainless steels under BWR environments [49], may be disregarded. Regarding the secondary oxide, the EDS signal demonstrates a sole iron-rich oxide with slight traces of Ni. Therefore, the single reasonable candidate structure is the nickel-bearing magnetite spinel oxide $(Fe_{1-x},Ni_x)_3O_4$, likewise featuring an fcc lattice with a lattice constant of 0.8338 nm [50], see Figs. 4E-F. The iron-nickel ratio may vary between Fe2 - Ni ($x \approx 0.33$) to Fe2.6 - Ni0.4 ($x \approx 0.13$) without reasonable change in the lattice structure. This change may be related to the local alloy composition, the oxygen diffusion and metal dissolution rates. The oxide compositions are in complete agreement with previous observations regarding SCC cracking in stainless steels [25, 29].

3.2. Crack tip analyzes

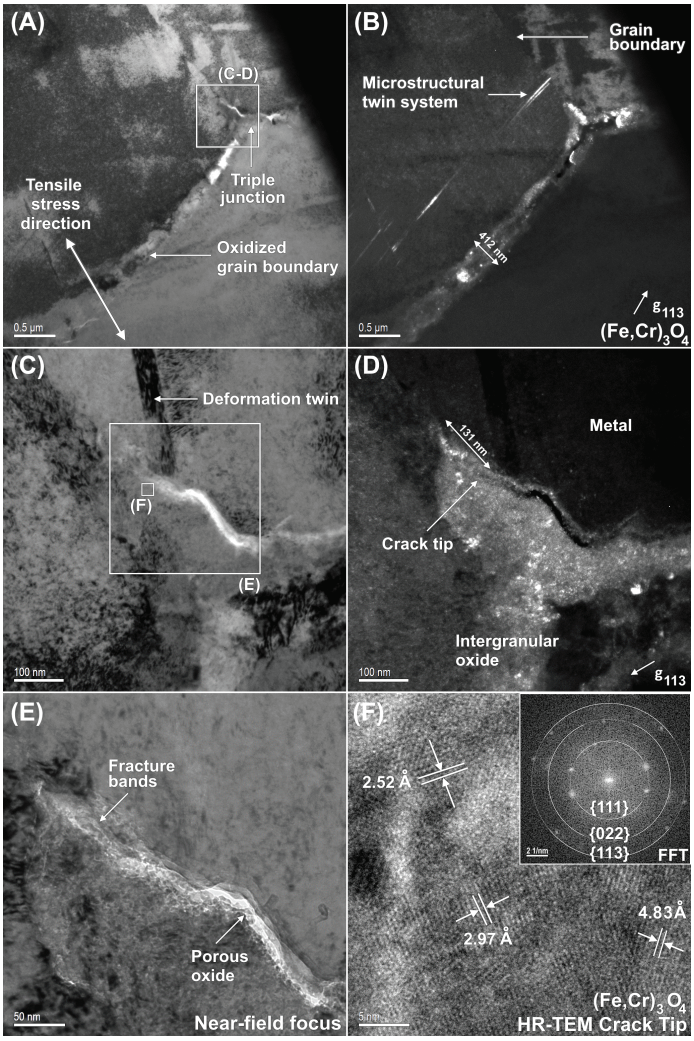

Figure 5: TTO-1-053 L03 (A) BF-TEM imaged IASCC intergranular crack propagating along an oxidized grain boundary, also seen in Fig. 2C. (B) Corresponding DF-TEM from an inner oxide reflection. (C) BF-TEM crack tip extending from the triple junction illustrating the presence of deformation twinning at the crack tip. (D) Corresponding DF-TEM illustrating the extent of intergranular oxide penetration in front of the crack tip. (E) BF-TEM underfocus Fresnel contrast image of the same crack tip from edge-on orientation. (F) HR-TEM of the oxide near the crack tip seen in (C), with a reduced FFT diffractogram as an inset matching the largest d-spacings of the chromite.

IASCC crack tips were either observed extending from beyond branched oxi-
330 dized triple junctions, or at the end of converged intergranular cracks, see Figs. 5A-B and 6A respectively. Most crack tips showed similar characteristics in

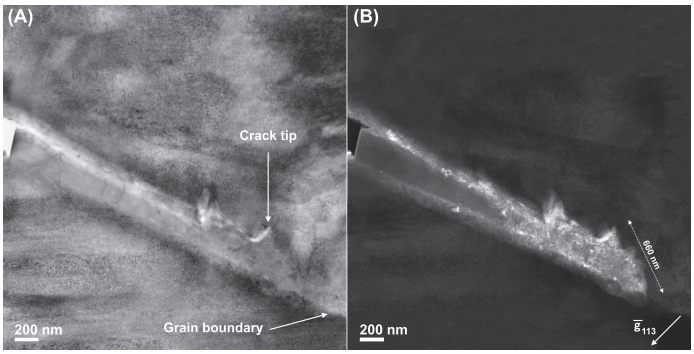

Figure 6: TTO-1-053 L08 (A) BF-TEM, and (B) corresponding DF-TEM of the integral chromite oxide, of an IASCC crack tip propagating along an oxidized grain boundary.

terms of morphology and surrounding microstructure. Oxide-filled grain boundaries taper down towards the advanced crack tip, often accompanied by strong deformation fields on either side of the grain boundary. Extensive deformation structures such as deformation-induced twins are visible when the adjacent grain boundary is tilted in suitable orientation, see Fig. 5C. Distinctive features include the oxide intrusion from the leading grain boundary facing the crack tip towards one of the neighboring grains, and the preferential cracking of the oxide along the metal-oxide interface.

Intergranular oxide penetration in front of the crack tip was consistently observed by performing SAED imaging of the crack tip oxide, see Figs. 5D and 6B. This oxide ingress may span distances of hundreds of nm's in front of the propagating crack tip. Several tips additionally showed porous structures within this leading crack tip oxide. Consequently, further investigation was performed from edge-on orientation using near-field Fresnel contrast imaging. Fig. 5E illustrates the porosity of the intergranular oxide which can be clearly seen adjacent to the crack flanks and leading crack tip edges near the metal interface. In front of the crack tip, noticeable fine fracture bands may be observed that represent the formation of brittle microcracks within the oxide-filled regions. These fracture bands propagate straight to the furthest intergranular oxide tip. HR-TEM examination of the oxide structure in front of the crack tip revealed that the leading crack tip oxide matches the previously found chromite observed along the crack flanks, see Fig. 5F. The inset FFT diffractogram illustrates reflections that match the largest lattice spacings of said chromite along the crack flanks.

3.3. Microstructural features

3.3.1. Crack deformation field

Two representative examples of BF-TEM imaged IASCC cracks are displayed in Figs. 7A and 4A. In analyzing the deformed microstructure, long-running

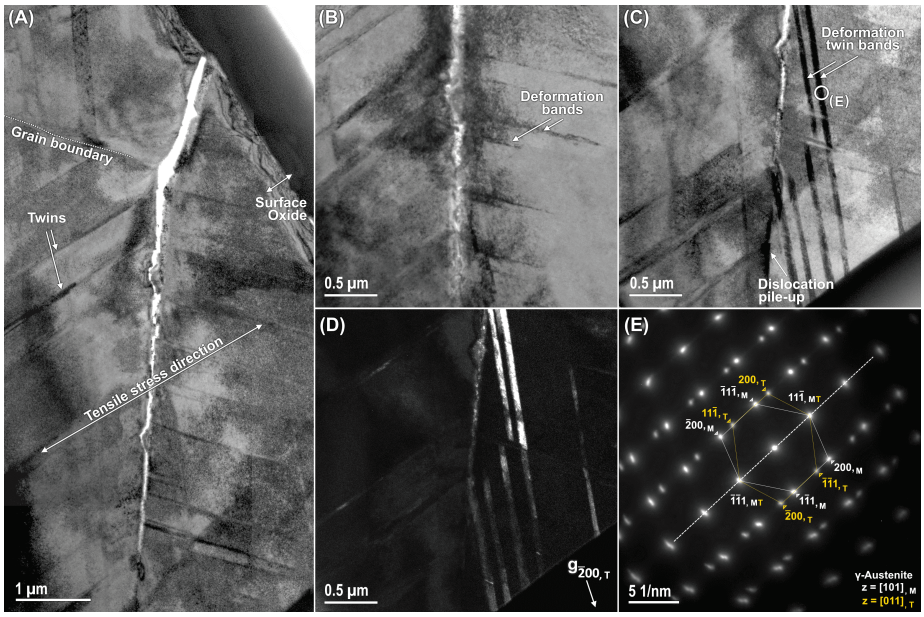

Figure 7: TTO-1-053 L05 (A) BF-TEM overview of a typical intergranular IASCC crack extending into the bulk. (B,C) BF-TEM deformation structures identified as deformation band and twin bands, respectively. (D) Corresponding DF-TEM, and (E) diffraction pattern of the deformation twin bands.

parallel deformation bands may be observed extending from the crack flanks and tip towards nearing grain boundaries, see Figs. 7B-C. Analysis of these deformation structures was performed through SAED imaging. When tilted into suitable orientation, it was observed that certain bands extending from the crack flanks could not be related to twinning while others that extended from the crack tip typically showed twin-related streak diffraction patterns, see Figs. 7B and 7C-E respectively. Consequently, these deformation structures were identified as general deformation and deformation twin bands accordingly.

Consistent with previous studies [21, 51], the observations of these linear defects are seemingly related to the crack initiation and propagation along the grain boundary. Deformation bands accumulate a high number of dislocations along specified crystallographic planes of the crystal lattice, and may nucleate as a result of increased external stresses induced by the crack propagation. To that respect, the deformation bands are frequently observed adjacent to the crack flanks. At the same time, the density of deformation twin bands generally increases closer towards the propagating intergranular crack. Similarly, this suggests the nucleation of deformation twins as a consequence of the crack propagation. However, it should be noted that an increased stress concentration caused by the twin-grain boundary interaction assists intergranular failure prior to crack formation [51]. In other words, deformation twins intercepted

by a grain boundary can act as preferential crack initiation sites and serve as to facilitate crack propagation. Apart from the extending deformation twins, an additional characteristic to consider is also the pile-up of dislocations at the leading grain boundary, see Fig. 7C. Especially in highly irradiated materials where defects play a significant role, dislocation build-up may produce additional internal stresses due to slip interaction with the grain boundary. This stress interaction can also be regarded as a prelude to intergranular failure, and acts as a consequence of grain boundary sliding due to dislocation absorption in front of the leading crack tip [52].

3.3.2. Martensitic transformation

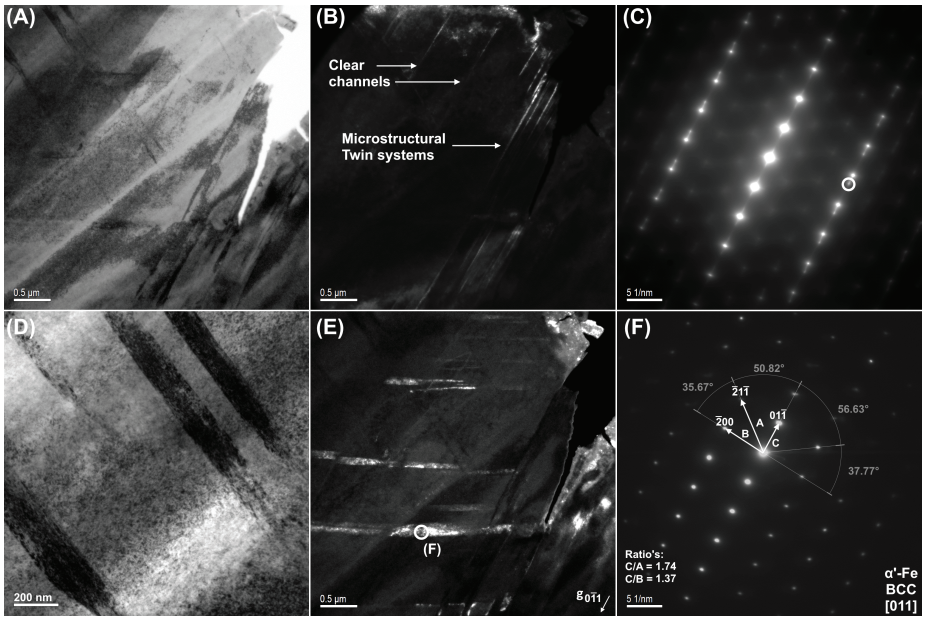

Figure 8: TTO-1-053 L06 (A) BF-TEM overview of the microstructure alongside a crack. (B) DF-TEM of microstructural twins extending from the crack flanks. (C) Corresponding diffraction pattern of twinned structure. (D) Magnified BF-TEM of stress-induced martensitic laths. (E) DF-TEM of laths extending from the crack tip. (F) Corresponding martensitic diffraction pattern illustrating the bcc-nature of the stress-induced α'-martensite from a [011] zone-axis.

Interestingly, aside to typical intergranular crack, notable microstructural defect structures can be observed. On the one hand, Figs. 4A-C depict the formation of microstructural twin systems and their corresponding low-symmetry diffraction pattern. On the other hand, thick deformation laths are occasionally present both within the bulk matrix and extending from the crack tip into the grain interior, see Figs. 8D and 8E-F respectively. Closer inspection of these laths was performed through SAED imaging. Fig. 8F indicates that the thick laths

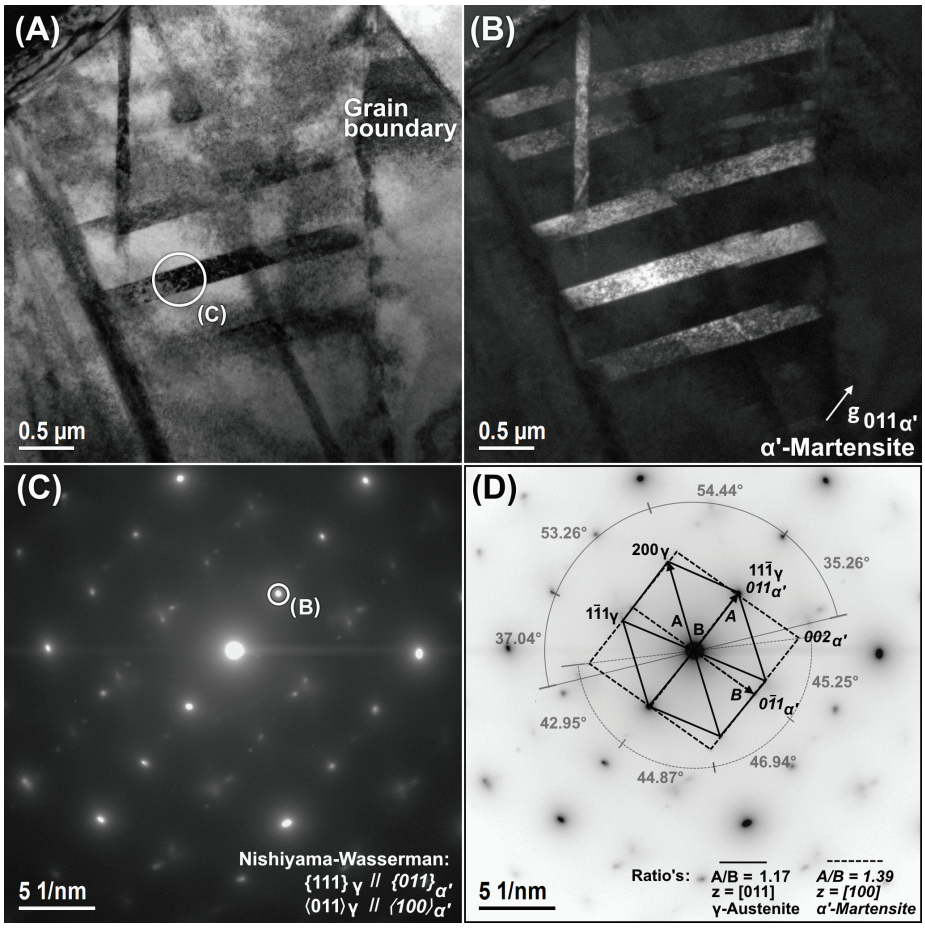

Figure 9: TTO-1-053 L05 (A) BF-TEM and (B) corresponding DF-TEM of martensitic laths extending across the grain close to the crack initiation. (C) Corresponding diffraction pattern of the martensitic laths. (D) Analyzed diffraction pattern matching the Nishiyama-Wasserman orientation relationship between fcc γ- austenite and bcc α'-martensite.

do not show a twin-related diffraction pattern. Rather, it is conceivable that the lattice locally transformed from the parent austenitic fcc nature towards a bcc centering, suggested by the altered interplanar ratios indicated in the diffraction pattern. In that sense, the microstructure sustained a structural transformation to a lattice that correlates well with deformation-induced α'-martensite. Such martensitic laths were commonly observed throughout this work, extending from the crack flanks and leading grain boundaries, propagating across the grain away from the propagating crack.

Other instances of martensitic phase transformation are displayed in Figs. 9 and 10. Thick laths are formed across the grain and intersect on either side of the

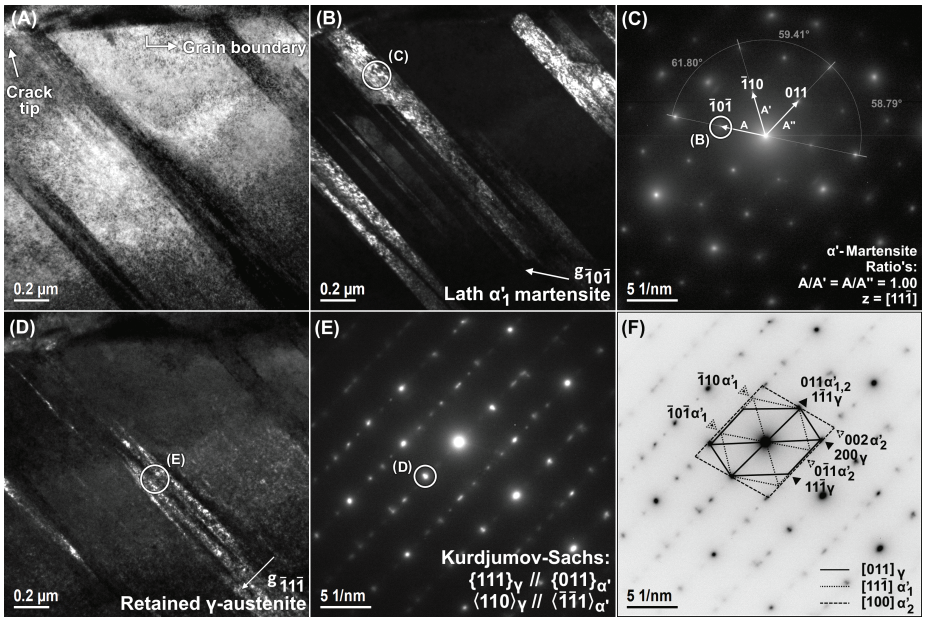

Figure 10: TTO-1-053 L05 (A) BF-TEM and (B,C) corresponding DF-TEM with associated diffraction pattern of α-martensite extending from the leading grain boundary in $[\bar{1}11]\alpha$ zone-axis orientation. (D,E) Retained γ-austenite located at martensite interfaces with associated diffraction pattern. (F) Analyzed diffraction pattern matching the Kurdjumov-Sachs orientation relationship between fcc γ- austenite and bcc α'-martensite.

grain boundary, see Fig. 9A. The following martensitic transformation occurs in close vicinity of the crack initiation point at the specimen surface. Suggested by the darker contrast regions at the grain boundary, dislocation pile-up in-between the intersections of the martensite with the grain boundary is present. The latter may suggest an impeding dislocation motion which may well induce local stress at the grain boundary. The additional reflections that appear in the diffraction pattern illustrated in Fig. 9C closely match the well-known Nishiyama-Wasserman (N-W) orientation relationship [33, 35] between fcc γ-austenite and bcc α'-martensite. Correspondingly, this shows that deformation-induced martensite nucleates along the close-packed crystallographic planes of austenite since both phases appear parallel in the zone-axis diffraction pattern:

$$\{111\}_\gamma \parallel \{011\}_{\alpha'}, (Nishiyama - Wasserman, Fig.9D)$$
$$< 011 >_\gamma \parallel < 100 >_{\alpha'}$$

Displayed in Fig. 10A-B, similar martensitic lath structures are unmistakably observed extending from the propagating crack tip and leading grain boundary. Once again, the high density of dislocation regions in-between the parent

austenite phase at the grain boundary seem to be a reoccurring characteristic. SAED imaging confirms the $[\bar{1}11]$ bcc nature of the martensite in Fig. 10C. However, in this instance, it is apparent from the corresponding DF-TEM view that an additional phase structure is present. As shown in Figs. 10F, analysis of the complementary diffraction pattern reveals the presence of an additional $[100]\alpha'$-martensitic lath accompanied by reflections corresponding to thin retained austenite. As depicted in Fig. 10D using the $(\bar{1}1\bar{1})\gamma$ reflection, the fcc austenite phase is located at the interfaces of the martensitic transformation. Considering one martensitic crystal at a time, Fig. 10F demonstrates the previously observed N-W orientation relationship between $[011]_\gamma \parallel [100]_{\alpha'}$ and the Kurdjumov-Sachs (K-S) orientation relationship between $[011]_\gamma \parallel [11\bar{1}]_{\alpha'}$. Considering that the N-W and K-S orientation relationships are related by 5.26° rotation, it is not surprising to observe both relationships together [53].

$$\{111\}_\gamma \parallel \{011\}_{\alpha'}, (Kurdjumov - Sachs, Fig.10F)$$
$$< 110 >_\gamma \| < \bar{1}\bar{1}1 >_{\alpha'}$$

In the case of austenitic steels, plastic deformation generally occurs either through the classic dislocation motion or through stringent lattice translations such as deformation-induced twinning and phase transformations. The competition is considered largely to be a thermodynamical driven process which is dependent on the material properties. The observation of martensite in close vicinity to intergranular crack at high-temperature water conditions is a remarkable feature in the sense that such phase transformations are more commonly reported at and below room temperatures [36]. However, in agreement with the literature, Bruemmer et al. [17] reported possible martensite formation consistent with their microstructural findings of intergranular cracks in SS304 and SS316 exposed to simulated BWR environments. Karlsen et al. [30] observed the indirect formation of α'-martensite through the intermediate hcp ϵ-martensite in strained SUS304 exposed to a simulated PWR environment. In that context, the nucleation of martensite has been largely attributed to the loss of nickel as an austenitic stabilizator in the matrix as a consequence of RIS at the grain boundaries. In the current case, α'-martensitic laths were primarily observed extending from the crack tip and leading grain boundary without evidence for the intermediary hcp ϵ-martensite. It is unlikely that the observed martensite formation is related to initial cold-work or as an artefact of the specimen preparation. Rather, it is reasoned that its formation is associated with large lattice deformations inherent to the crack propagation, a process which is stress-assisted at the crack tip. From this perspective, other studies pointed out the stress-assisted dependency of bcc phase-transformations [54, 55, 56], an aspect that is under the current circumstances relevant close to crack initiation and propagation. After nucleation, the finite-volumes of martensite may significantly affect the bulk mechanical properties. Martensitic transformation is known to impede on the dislocation motion which can imply a localized increase in hardening. Figs. 9A and 10A clearly illustrate substantial regions of highly

dislocated structures in-between the intersections of the martensitic laths with the grain boundaries. The following can be linked to the lack of dislocation glide and the inadequate strain to nearby slip planes. In that sense, martensitic transformation may cause an effective increase in strain-hardening that can lead to an increased cracking susceptibility [30, 37].

3.4. Intrinsic causes of crack arrest

3.4.1. MnS inclusion particles

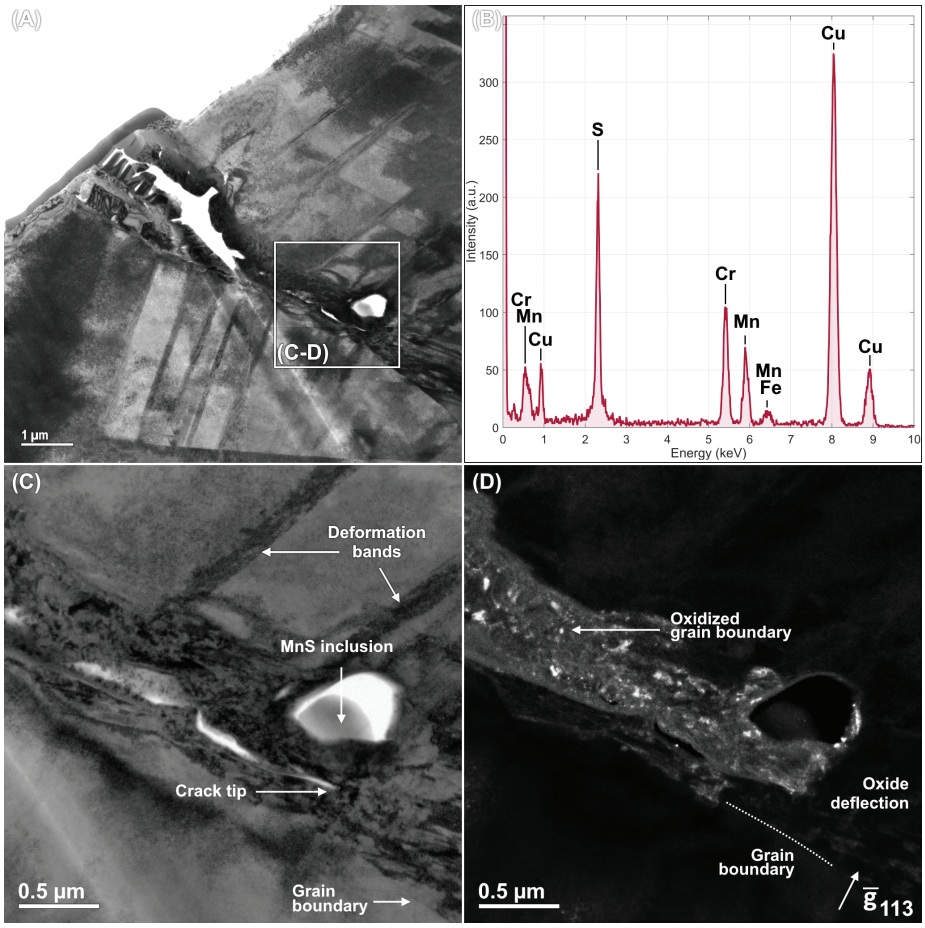

Figure 11: TTO-1-053 L01 (A) BF-TEM of an intergranular IASCC crack arrested at a (B) EDS-confirmed MnS inclusion particle in close vicinity to the grain boundary. (C) BF-TEM of the crack tip illustrating a heavy deformation field in close vicinity to the particle. (D) DF-TEM displaying the intergranular oxide deflection away from the grain boundary towards the inclusion particle.

Fig. 11A depicts an overview of an IASCC crack that has clearly arrested at an

intergranular inclusion particle. Close consideration of the chemical structure of the inclusion particle is presented by the corresponding EDS spectrum in Fig. 11B. The spectrum exhibits strong peaks which can be assigned to Mn, S and Cu. As a result, the particle is further referred to as being a MnS inclusion particle, in correspondence to the literature nomenclature [57, 58, 59]. The inclusion particle has segregated close to the grain boundary, altering the crack path and ultimately arresting the IASCC crack. As shown in Figs. 11C-D, it is evident how the oxidation deflects from the leading grain boundary, encapsulating the inclusion. The arrest is accompanied with strong lattice deformation, suggested by the dense deformation field ahead of the crack and the propagation of deformation slip bands from the crack flanks. Interestingly, the intersections of the deformation bands with the crack led to a discontinuous ingress of oxide into the bulk matrix. In association with earlier findings [22, 60, 23], deformation bands may act as fast-diffusion paths for intergranular oxidation. The ingress along the deformation slip bands is reasonably facilitated by the localized dislocation flow in the highly deformed microstructure close to the crack flanks.

Manganese is added to steel to stabilize the austenitic structure since it, together with Ni, guarantees a complete austenite formation during the austenization treatment [61]. Sulfur on the other hand, commonly binds with Mn in the form of manganese sulfides, to act as a source of stress concentrator which favors the steel's machinability by reducing the cutting force [62]. However, considering the recurrent observations of surface pitting corrosion at MnS particles [58, 63, 64], degrading corrosion properties should be expected as a consequence of an increasing sulfur content. Therefore, the addition of S should be considered as a trade-off between the material's performance and its corrosion qualities. Nonetheless, regarding intergranular crack propagation, the role of bulk segregated MnS inclusions remained undetermined. Since MnS inclusions are in principle less noble than the surrounding matrix [57], it can be expected that these particles would preferentially oxidize and dissolve under high-temperature water conditions when coming into contact with an intergranular crack. However, from Fig. 11 it is evident that the particle actively impedes further grain boundary failure. In fact, coupled with the localized deformation slip bands close to the crack, the intergranular oxidation is solely corroding the metallic matrix around the inclusion. Altogether, from these observations, it is clear that MnS inclusions have a retarding effect what concerns intergranular crack propagation.

3.4.2. Tensile stress direction

Generally, the role of the external tensile stress with respect to intergranular cracking is made evident under general examination of several fractured grain boundaries. Relative to the orientation of the grain boundary, especially following triple junctions where one of the boundaries failed preferentially compared to the other, it was observed that the cracking typically aligned perpendicular towards the external tensile stress direction. As observed in Fig. 12A-B and

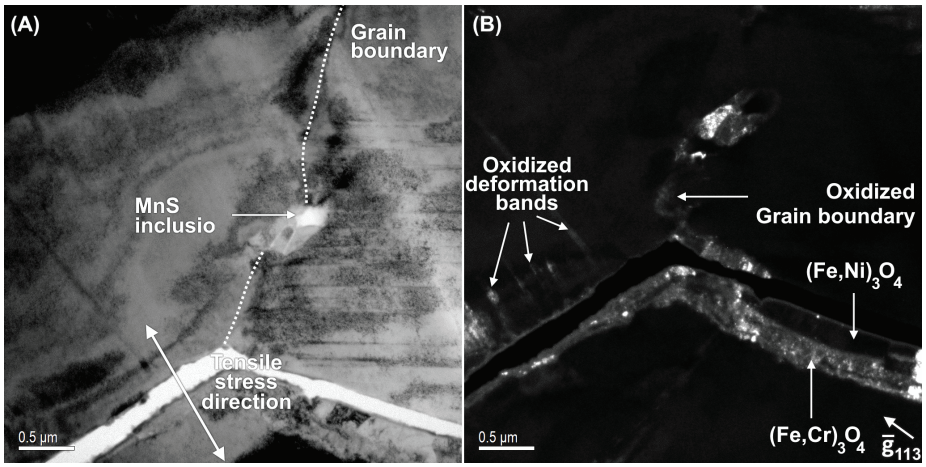

Figure 12: TTO-1-053 L03 (A) BF-TEM of an intergranular crack propagating in cleavage mode in relation to the tensile stress direction. (B) DF-TEM of oxidized grain boundary triple junction. (C-D) DF-TEM of the opposing grains.

Tab. 3, cracks propagating beyond an oxidized triple junction tend to always follow a crack path in cleavage mode orientation, even though the adverse grain boundary was equally oxidized. In agreement with previous studies associating the tensile stress to crack propagation [51], this result indicates external tensile stress assists intergranular cracking most effectively whenever both the grain boundary normal and the stress orientation are aligned in parallel. In all other cases, the crack propagation was shortly followed by a full crack arrest.

Additionally, it was observed that deformation bands departing from the crack flanks preferentially oxidize whenever the stress-orientation was parallel. Confirmed by EDS spectra, the oxidation along such deformation bands reached transgranular lengths of up to several hundreds of nm's where the bands are parallel towards the external stress. This form of stress-assisted oxidation nicely corresponds to the findings reported by Lozano-Perez et al. [60].

3.5. STEM-HAADF analyzes

RIS occurs at microstructural free surfaces acting as defect sinks, such as grain boundaries, dislocations, and precipitate interfaces and is assisted by neutron-irradiation. With the focus on IASCC cracking, the chemical composition of unimpaired grain boundaries was analyzed using STEM-HAADF EDS line scans. Chemical composition profiles of IASCC crack tips are additionally reported.

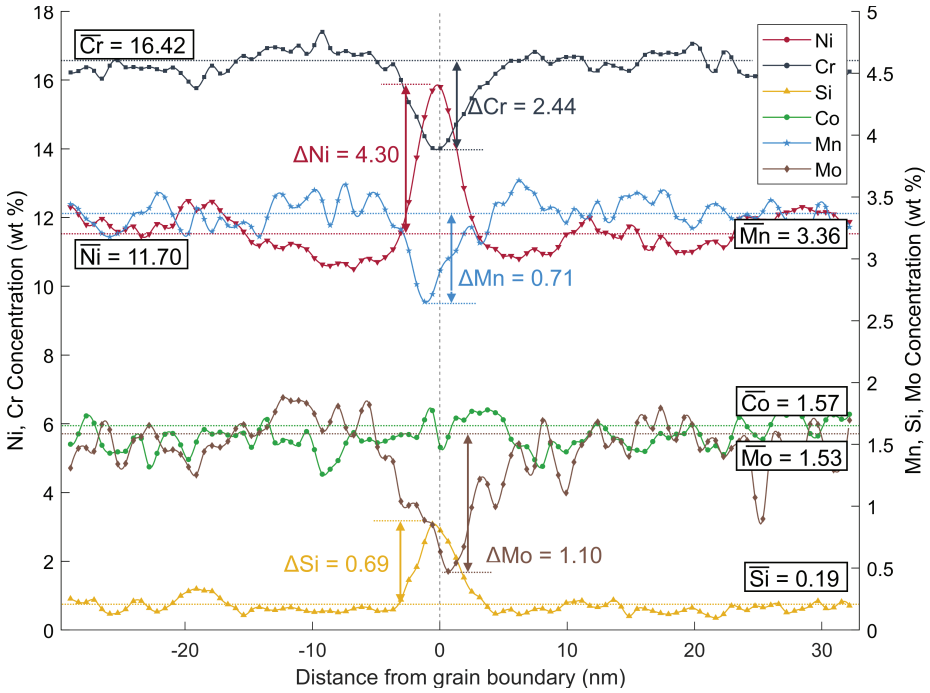

Figure 13: TTO-1-053 L08 HAADF-STEM EDX line scan of edge-on unimpaired grain boundary triple junction.

3.5.1. RIS at unimpaired grain boundaries

Thorough analysis of the chemical composition of an unimpaired grain boundary close to a triple junction is displayed in Fig. 13. Segregation and depletion of several elements are evident from the edge-on orientated grain boundary profile. Ni and Si are unmistakably enriched versus the clear depletion of Cr, Mn and Mo. Ni is considered as the slowest diffusing element, reaching segregation levels of up to 16 wt.% enrichment at the grain boundary (36% increase). On the other hand, Cr depletes to a value of about 14 wt.% compared to the structural matrix composition (17% decrease). Pre-depletion and -segregation of respectively Ni and Cr are apparent by the narrow regions of change adjacent to the grain boundary. Considering the high irradiation exposure (60 dpa; neutron-irradiated), this pre-depletion and -segregation may suggest an interaction between other co-diffused elements. Correspondingly, the depletion of other alloying elements like Mn and Mo is also observed. Bruemmer et al. [4] argued that Mn, similarly as to Mb, deplete on the basis of both strong diffusion and transmutation at high fluence levels but neither has been implicated to play a major role for crack initiation. With respect to the role of Si, which was found to be enriched up to five times along the current grain boundary, its implication on crack initiation is not yet fully understood [13].

The rate of change of the RIS profile is consistent with the inverse Kirkendall mechanism [65], and is slightly enhanced compared to the segregation profiles presented for low-to-moderate fluences in the literature [4, 13]. As for reference, the average element composition distant from the grain boundary closely corresponds to the bulk matrix composition. In that sense, it is estimated that the diffusion length of both structural and solute elements is of the order of tens of nm's.

3.5.2. STEM-HAADF mapping

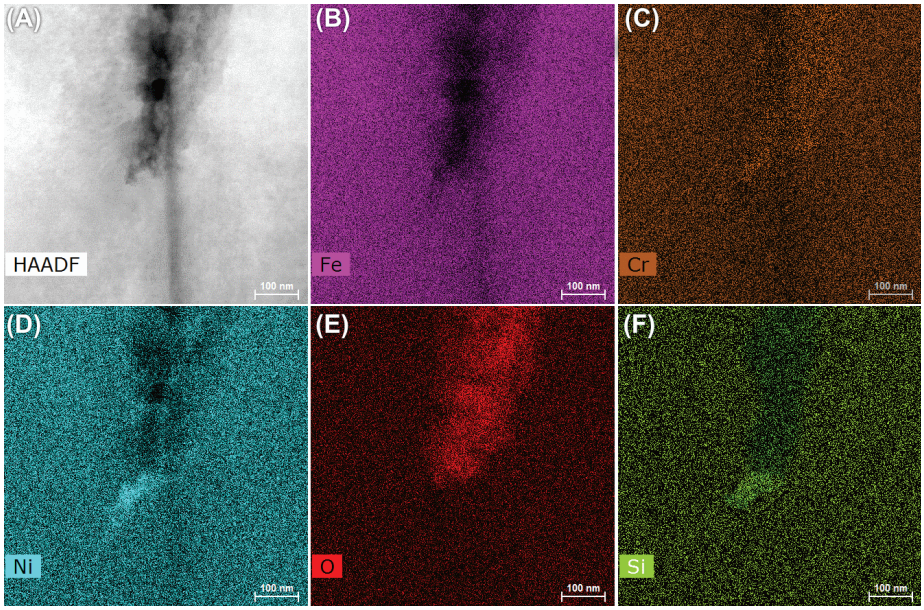

Figure 14: TTO-1-053 L08 HAADF-STEM EDS chemical mapping of enriched and depleted elements close to a selected IASCC crack tip.

Fig. 14 demonstrates the most relevant STEM-EDS maps of an impaired GB branching from a main IASCC crack. A highly Ni-enriched metallic zone on one specific side of the grain boundary was observed, spanning a range of approximately 70 nm wide and 75 nm in front of the crack tip. Additionally, preferential segregation of solute elements such as Si is apparent close to the crack tip. In that respect, the element composition of the leading grain boundary in front of the crack tip is expected to be highly altered.

3.6. IASCC cracking mechanisms

From the observation of thin fracture bands within the intergranular oxide structure of the leading crack tip, it is reasoned that the oxide parameters play a dominant role in terms of general crack initiation. Brittle fracture bands may

nucleate as a consequence of the fine oxide porosity, which can be associated with the microcrack coalescence mechanism. These findings are in good agreement with the so-called subcritical crack propagation (SCP) process proposed to be relevant for IASCC by Konstantinović [39]. This model is based on the internal oxidation model [8, 26, 45, 46, 47]. Accordingly, the SCP model describes a slow crack growth under an applied stress well below the critical value for oxide rupture, which is pre-determined by an intrinsic failure probability of the intergranular oxide itself and its bonding with the metal interface. Given the observation of multiple crack initiation sites within the oxide, the underlying assumption for a failure probability that drives the crack initiation process is rather conceivable. The failure probability successfully explains the observation of multiscale fracture bands within the oxide, as is displayed in Fig. 5E. Interestingly, our observations also associate well with the crack coalescence mechanism proposed by Lu et al. [49], wherein the main crack advances through coalescence of the microcrack fracture bands. According to their observations, the nucleation and growth of fracture bands into fully developed microcracks provide fast-diffusion paths for oxide diffusion ahead of the propagating crack tip. Subsequent linkage of the microcracks assisted by external loading propagates the crack further forward. Altogether, both models associates equally well our observations.

4. Conclusions

This study performed a microstructural investigation on IASCC cracks in a 316SS neutron-irradiated (60 dpa) O-ring specimen, extracted from the in-service flux thimble tube of the Tihange PWR. Several intergranular cracks were investigated using FIB sample preparation and consequent TEM analysis, from which the following may be concluded:

(i) Internal oxidation of leading grain boundaries has been illustrated by distinct oxidation in front of propagating crack tips, accompanied by thin oxide fracture bands in front of the crack tip and preferential cracking in between the metal-oxide interface. All findings fully support the IASCC model based on subcritical crack propagation [39] in oxidized grain boundaries.

(ii) Extensive deformation structures, including twin-deformation and deformation slip bands, were observed in the near vicinity of the intergranular cracks and crack tips. Additionally, crack tip propagation is accompanied by definite strain-induced martensite phase transformation $\gamma \rightarrow \alpha$'), consistent with corresponding Nishiyama-Wasserman and Kurdjumov-Sachs orientation relationships observed in detailed diffraction pattern analyses. Suggested by the repeated findings of martensite laths extending from the crack tips and leading grain boundaries, it is credible that these phase transitions were stress-induced on the account of extensive lattice

deformations, rather than during initial cold-work or as an artefact of the specimen preparation.

(iii) Crack flanks display the formation of a duplex oxide consisting of a nano-grained primary chromite and secondary magnetite oxide, which were considered to be the resultant of corrosion-oxidation and precipitation processes, respectively.

(iv) RIS was observed along unimpaired grain boundaries, showing signs of strong Cr-, Mn- and Mo-depletion in addition to Ni- and Si-enrichment.

(v) MnS inclusion particles segregating close to the fractured grain boundary have been found to imply a retarding effect on IASCC crack propagation. With respect to the aspect of external tensile stress, cracking typically follows a crack path in cleavage mode orientation wherein the external tensile stress assists intergranular cracking most effectively when both the grain boundary normal and the stress orientation are aligned in parallel.

Acknowledgements

This work is supported by ENGIE Electrabel under grant agreement No. BENGIE5500, and by the EMAT research group from the University of Antwerp.

References

[1] P. Scott. 2000 F.N. speller award lecture: Stress corrosion cracking in pressurized water reactors interpretation, modeling, and remedies. *Corrosion*, 56, 08 2000.

[2] P L Andresen. Emerging issues and fundamental processes in environmental cracking in hot water. *Corrosion*, 64(5):439–464, 2008.

[3] G. S. Was and P. L. Andresen. Stress corrosion cracking behavior of alloys in aggressive nuclear reactor core environments. *Corrosion*, 63(1):19–45, 2007.

[4] S. M. Bruemmer, E. P. Simonen, P. M. Scott, P. L. Andresen, G. S. Was, and J. L. Nelson. Radiation-induced material changes and susceptibility to intergranular failure of light-water-reactor core internals. *Journal of Nuclear Materials*, 274(3):299–314, 1999.

[5] O.K. Chopra and A.S. Rao. Degradation of LWR core internal materials due to neutron irradiation, NUREG/CR-7027. 2010.

[6] Gary S Was, Yugo Ashida, and Peter L Andresen. Irradiation-assisted stress corrosion cracking. *Corrosion Reviews*, 29(1-2):7–49, 2011.

[7] O. K. Chopra and A. S. Rao. A review of irradiation effects on LWR core internal materials - IASCC susceptibility and crack growth rates of austenitic stainless steels. *Journal of Nuclear Materials*, 409(3):235–256, 2011.

[8] Sergio Lozano-Perez, Judith Dohr, Martina Meisnar, and Karen Kruska. SCC in PWRs: Learning from a Bottom-Up Approach. *Metallurgical and Materials Transactions E*, 1(2):194–210, 2014.

[9] Anna Hojná. Overview of Intergranular Fracture of Neutron Irradiated Austenitic Stainless Steels. *Metals*, 7(10):392, 2017.

[10] Gary S. Was and Peter L. Andresen. *Mechanisms behind irradiation-assisted stress corrosion cracking*. LTD, 2020.

[11] G.S. Was and P.L. Andresen. 6 - irradiation assisted corrosion and stress corrosion cracking (iac/iascc) in nuclear reactor systems and components. In Damien Féron, editor, *Nuclear Corrosion Science and Engineering*, Woodhead Publishing Series in Energy, pages 131–185. Woodhead Publishing, 2012.

[12] Stephen M Bruemmer and Gary S Was. Microstructural and microchemical mechanisms controlling intergranular stress corrosion cracking in light-water-reactor systems. *Journal of Nuclear Materials*, 216:348–363, 1994.

[13] J. T. Busby, G. S. Was, and E. A. Kenik. Isolating the effect of radiation-induced segregation in irradiation-assisted stress corrosion cracking of austenitic stainless steels. *Journal of Nuclear Materials*, 302(1):20–40, 2002.

[14] G. F. Li, Y. F. Kaneshima, and T. Shoji. Effects of impurities on environmentally assisted crack growth of solution-annealed austenitic steels in primary water at 325°C. *Corrosion*, 56(5):460–469, 2000.

[15] Hiromasa Nishioka, Koji Fukuya, Katsuhiko Fujii, and Yuji Kitsunai. Deformation structure in highly irradiated stainless steels. *Journal of Nuclear Science and Technology*, 45(4):274–287, 2008.

[16] Z. Jiao and G. S. Was. Localized deformation and IASCC initiation in austenitic stainless steels. *Journal of Nuclear Materials*, 382(2-3):203–209, 2008.

[17] Stephen M. Bruemmer and Larry E. Thomas. High-resolution characterizations of stress-corrosion cracks in austenitic stainless steel from crack growth tests in BWR-simulated environments. *Proceedings of the Twelfth International Conference on Environmental Degradation of Materials in Nuclear Power Systems-Water Reactors*, pages 189–198, 2005.

[18] Legras Laurent, Boisson Marylou, Fargeas Elodie, Cuvillier Priscille, Mercier Rémi, E D F D P N Unie, and Pleyel Saint-denis. TEM investigations of the microstructure and oxides at the tip of intergranular cracks of a baffle former bolt irradiated up to 10 dpa. (September), 2018.

[19] Takuya Fukumura, Koji Fukuya, Katsuhiko Fujii, Terumitsu Miura, and Yuji Kitsunai. Grain boundary oxidation of neutron irradiated stainless steels in simulated pwr water. *Minerals, Metals and Materials Series*, pages 2153–2163, 2019.

[20] Donghai Du, Kai Sun, and Gary S Was. Materials Characterization IASCC of neutron irradiated 316 stainless steel to 125 dpa. *Materials Characterization*, 173(January):110897, 2021.

[21] T. Onchi, K. Dohi, N. Soneda, J. R. Cowan, R. J. Scowen, and M. L. Castaño. Fractographic and microstructural characterization of irradiated 304 stainless steel intergranularly fractured in inert gas. *Journal of Nuclear Materials*, 320(3):194–208, 2003.

[22] Sergio Lozano-Perez, David W. Saxey, Takuyo Yamada, and Takumi Terachi. Atom-probe tomography characterization of the oxidation of stainless steel. *Scripta Materialia*, 62(11):855–858, 2010.

[23] F. Scenini and A. Sherry. Stress corrosion cracking of sensitized type 304 stainless steel in high-temperature water with anionic impurities contamination. *Corrosion*, 68(12):1094–1107, 2012.

[24] Sergio Lozano-Perez, Karen Kruska, Ilya Iyengar, Takumi Terachi, and Takuyo Yamada. The role of cold work and applied stress on surface oxidation of 304 stainless steel. *Corrosion Science*, 56:78–85, 2012.

[25] Xiaolong Liu, Woonggi Hwang, Jaewoong Park, Donghyun Van, Yunlong Chang, Seung Hwan Lee, Sung Yup Kim, Sangsoo Han, and Boyoung Lee. Toward the multiscale nature of stress corrosion cracking. *Nuclear Engineering and Technology*, 50(1):1–17, 2018.

[26] Sergio Lozano-perez, Martina Meisnar, and Judith Dohr. Reviewing the internal oxidation mechanism as a plausible explanation for SCC in PWR primary water . (August), 2013.

[27] CRITICAL ANALYSIS OF " TIGHT CRACKS " Roger W . Stachle years of studies of stress corrosion cracking (SCC) using the Analytical mainly Fe-Cr-Ni alloys of types used in water cooled nuclear power plants in.

[28] Takumi Terachi, Katsuhiko Fujii, and Koji Arioka. Microstructural characterization of scc crack tip and oxide film for SUS 316 stainless steel in simulated PWR primary water at 320°C. *Journal of Nuclear Science and Technology*, 42(2):225–232, 2005.

[29] Karen Kruska, Sergio Lozano-perez, David W Saxey, Takumi Terachi, Takuyo Yamada, and George D W Smith. Nanoscale characterisation of grain boundary oxidation in cold-worked stainless steels. *Corrosion Science*, 63:225–233, 2012.

[30] Wade Karlsen, Janne Pakarinen, Aki Toivonen, and Ulla Ehrnstén. DEFORMATION MICROSTRUCTURES OF 30 dpa AISI 304 STAINLESS STEEL AFTER MONOTONIC TENSILE AND CONSTANT LOAD AUTOCLAVE TESTING. 2011.

[31] Wade Karlsen, Aki Toivonen, and Pål Efsing. Baseline Examinations and Autoclave Tests of 65 and 100 dpa Flux Thimble Tube O-Ring Specimens. 2:248–273, 2021.

[32] Ihho Park, Eun Young Kim, and Won Jon Yang. Microstructural investigation of stress corrosion cracking in cold-formed aisi 304 reactor. *Metals*, 11(1):1–10, 2021.

[33] K. Koumatos and A. Muehlemann. A theoretical investigation of orientation relationships and transformation strains in steels. *Acta Crystallographica Section A: Foundations and Advances*, 73:115–123, 2017.

[34] G. Kurdjumow and G. Sachs. Der Mechanismus der Stahlhärtung. *Die Naturwissenschaften*, 18(22):534, 1930.

[35] 2 - crystallography of martensite (general). In Morris E. Fine, M. Meshii, C.M. Wayman, and Zenji Nishiyama, editors, *Martensitic Transformation*, pages 14–134. Academic Press, 1978.

[36] Wade Karlsen, Gonzalo Diego, and Bastian Devrient. Localized deformation as a key precursor to initiation of intergranular stress corrosion cracking of austenitic stainless steels employed in nuclear power plants. *Journal of Nuclear Materials*, 406(1):138–151, 2010.

[37] Juho Talonen, Gersom Pape, and Delft Technology. Effect of Strain Rate on the Strain-Induced g S a ¿ -Martensite Transformation and Mechanical Properties of Austenitic Stainless Steels. (January 2016), 2005.

[38] R. W. Bosch, M. Vankeerberghen, R. Gérard, and F. Somville. Crack initiation testing of thimble tube material under PWR conditions to determine a stress threshold for IASCC. *Journal of Nuclear Materials*, 461:112–121, 2015.

[39] M. J. Konstantinović. Internal oxidation and probabilistic fracture model of irradiation assisted stress corrosion cracking in stainless steels. *Journal of Nuclear Materials*, 495:220–224, 2017.

[40] W. Van Renterghem, M. J. Konstantinović, and M. Vankeerberghen. Evolution of the radiation-induced defect structure in 316 type stainless steel after post-irradiation annealing. *Journal of Nuclear Materials*, 452(1-3):158–165, 2014.

[41] J. Conermann, R. Shogan, S. Yamaguchi, H Kanasaki, S. Nashida, K. Fujimoto, Y. Yamaguchi, and T. Yonezawa. Materials Reliability Program: Characterizations of Type 316 Cold Worked Stainless Steel Highly Irradiated Under PWR Operating Conditions (MRP-73), EPRI, Palo Alto, CA and MRP/International IASCC Committee. 3(3), 2002.

[42] A. Penders, M. J. Konstantinović, W. Van Renterghem, R.W. Bosch, and D. Schryvers. TEM investigation of SCC crack tips in high Si stainless steel tapered specimens. *Corrosion Engineering, Science and Technology*, 0(0):1–11, 2021.

[43] Tohru Ishitani, Kaoru Umemura, Tsuyoshi Ohnishi, Toshie Yaguchi, and Takeo Kamino. Improvements in performance of focused ion beam cross-sectioning: Aspects of ion-sample interaction. *Journal of Electron Microscopy*, 53(5):443–449, 2004.

[44] Thomas Henning Loeber, Bert Laegel, Sandra Wolff, Sebastian Schuff, Frank Balle, Tilmann Beck, Dietmar Eifler, Jan Henrik Fitschen, and Gabriele Steidl. Reducing curtaining effects in FIB/SEM applications by a goniometer stage and an image processing method. *Journal of Vacuum Science & Technology B, Nanotechnology and Microelectronics: Materials, Processing, Measurement, and Phenomena*, 35(6):06GK01, 2017.

[45] P.M. Scott and M. Le Calver. *Some possible mechanisms of intergranular stress corrosion cracking of Alloy 600 in PWR primary water*. Minerals, Metals ampersand Materials Society, 1993.

[46] P. M. Scott. An overview of internal oxidation as a possible explanation of intergranular stress corrosion cracking of alloy 600 in PWRS. *Proceedings of the Ninth International Symposium on Environmental Degradation of Materials in Nuclear Power Systems - Water Reactors* -, pages 3–14, 1999.

[47] Helen Dugdale, David E.J. Armstrong, Edmund Tarleton, Steve G. Roberts, and Sergio Lozano-Perez. How oxidized grain boundaries fail. *Acta Materialia*, 61(13):4707–4713, 2013.

[48] G. Shirane, D.E. Cox, and S.J. Pickart. Magnetic structures in FeCr2S4 and FeCr2 O4. *J. Appl. Phys.*, 35(2):954—955, 1964.

[49] Y H Lu. An ATEM study of oxidation behavior of SCC crack tips in 304L stainless steel in high temperature oxygenated water. 347:52–68, 2005.

[50] K. N. Subramanyam. Neutron and X-ray diffraction studies of certain doped nickel ferrites. *Journal of Physics C: Solid State Physics*, 4(15):2266–2268, 1971.

[51] Motomichi Koyama, Eiji Akiyama, Kaneaki Tsuzaki, and Dierk Raabe. Hydrogen-assisted failure in a twinning-induced plasticity steel studied under in situ hydrogen charging by electron channeling contrast imaging. *Acta Materialia*, 61(12):4607–4618, 2013.

[52] B. Alexandreanu and G. S. Was. Grain boundary deformation-induced intergranular stress corrosion cracking of Ni-16Cr-9Fe in 360°C water. *Corrosion*, 59(8):705–720, 2003.

[53] B V.N. Rao. On the orientation relationships between retained austenite and "lath" martensite.

[54] V. Tsakiris and D. V. Edmonds. Martensite and deformation twinning in austenitic steels. *Materials Science and Engineering A*, 273-275:430–436, 1999.

[55] Yongfeng Li, Fuming Bu, Wenbin Kan, and Hongliang Pan. Deformation-induced martensitic transformation behavior in cold-rolled aisi304 stainless steels. *Materials and Manufacturing Processes*, 28(3):256–259, 2013.

[56] G. B. Olson and Morris Cohen. Stress-assisted isothermal martensitic transformation: Application to TRIP steels. *Metallurgical Transactions A*, 13(11):1907–1914, 1982.

[57] G. Wranglen. Pitting and sulphide inclusions in steel. *Corrosion Science*, 14(5):331–349, 1974.

[58] R S Lillard, M A Kashfipour, and W Niu. Pit Propagation at the Boundary between Manganese Sulfide Inclusions and Austenitic Stainless Steel 303 and the Role of Copper Pit Propagation at the Boundary between Manganese Sulfide Inclusions and Austenitic Stainless Steel 303 and the Role of Copper. (January 2016), 2019.

[59] Mary P. Ryan, David E. Williams, Richard J. Chater, Bernie M. Hutton, and David S. McPhail. Why stainless steel corrodes. *Nature*, 415(6873):770–774, 2002.

[60] S. Lozano-Perez, T. Yamada, T. Terachi, M. Schröder, C. A. English, G. D.W. Smith, C. R.M. Grovenor, and B. L. Eyre. Multi-scale characterization of stress corrosion cracking of cold-worked stainless steels and the influence of Cr content. *Acta Materialia*, 57(18):5361–5381, 2009.

[61] Harshad Bhadeshia and Robert Honeycombe. Chapter 4 - solutes that substitute for iron. In Harshad Bhadeshia and Robert Honeycombe, editors, *Steels: Microstructure and Properties (Fourth Edition)*, pages 101–134. Butterworth-Heinemann, fourth edition edition, 2017.

[62] Yu Nan Wang, Jian Yang, and Yan Ping Bao. Effects of Non-metallic Inclusions on Machinability of Free-Cutting Steels Investigated by Nano-Indentation Measurements. *Metallurgical and Materials Transactions A: Physical Metallurgy and Materials Science*, 46(1):281–292, 2015.

[63] J. Stewart and D. E. Williams. The initiation of pitting corrosion on austenitic stainless steel: on the role and importance of sulphide inclusions. *Corrosion Science*, 33(3), 1992.

[64] Kale J Stephenson and Gary S Was. The role of dislocation channeling in IASCC initiation of neutron irradiated stainless steel. *Journal of Nuclear Materials*, 481:214–225, 2016.

[65] G S Was, M Atzmon, and E A Kenik. Microchemistry and microstructure of proton-irradiated austenitic alloys : toward an understanding of irradiation e ects in LWR core components. 270:96–114, 1999.